

Destruction of Kondo effect in cubic heavy fermion compound $\text{Ce}_3\text{Pd}_{20}\text{Si}_6$

J. Custers¹, K.-A. Lorenzer¹, M. Müller¹, A. Prokofiev¹, A. Sidorenko¹, H. Winkler¹, A. M. Strydom², Y. Shimura³, T. Sakakibara³, R. Yu⁴, Q. Si⁴, and S. Paschen^{1*}

¹ Institute of Solid State Physics, Vienna University of Technology, 1040 Vienna, Austria

² Physics Department, University of Johannesburg, Auckland Park 2006, South Africa

³ Institute for Solid State Physics, University of Tokyo, Kashiwa 277-8581, Japan

⁴ Department of Physics and Astronomy, Rice University, Houston, TX 77005, USA

* e-mail: paschen@ifp.tuwien.ac.at

How ground states of quantum matter transform between one another reveals deep insights into the mechanisms stabilizing them. Correspondingly, quantum phase transitions are explored in numerous materials classes, with heavy fermion compounds being among the most prominent ones. Recent studies in an anisotropic heavy fermion compound have shown that different types of transitions are induced by variations of chemical or external pressure¹⁻³, raising the question of the extent to which heavy fermion quantum criticality is universal. To make progress, it is essential to broaden both the materials basis and the microscopic parameter variety. Here, we identify a cubic heavy fermion material as exhibiting a field-induced quantum phase transition, and show how the material can be used to explore one extreme of the dimensionality axis. The transition between two different ordered phases is accompanied by an abrupt change of Fermi surface, reminiscent of what happens across the field-induced antiferromagnetic to paramagnetic transition in the anisotropic YbRh_2Si_2 . This finding leads to a materials-based global phase diagram – a precondition for a unified theoretical description.

Quantum phase transitions arise in matter at zero temperature due to competing interactions. When they are continuous, the associated quantum critical points (QCPs) give rise to collective excitations which influence the physical properties over a wide range of parameters. As such, they are being explored in a variety of electronic materials, ranging from high T_c cuprates to insulating magnets and quantum Hall systems^{4,5}.

Heavy fermion compounds are prototype materials to study quantum phase transitions. Their low energy scales allow to induce such transitions deliberately, by the variation of external parameters such as pressure or magnetic field. Microscopically, electrons in partially-filled f shells behave as localized magnetic moments. They interact with conduction electrons through a Kondo exchange interaction, which favors a non-magnetic ground state that entangles the local moments and the spins of the conduction electrons. They also interact among themselves through an RKKY exchange interaction, which typically induces antiferromagnetic order. The best characterized QCPs occur in heavy fermion compounds with anisotropic structures. Examples include the monoclinic $\text{CeCu}_{6-x}\text{Au}_x$ (ref. ⁶), and tetragonal CePd_2Si_2 (ref. ⁷), YbRh_2Si_2 (ref. ⁸) and CeMIn_5 ($M=\text{Co,Rh}$)⁹.

It has been known that tuning external parameters changes the ratio of the Kondo coupling to the RKKY interaction. Recently, the importance of a second microscopic quantity has been suggested. This is the degree of quantum fluctuations of the local moments, parameterized by G : magnetic order weakens with increasing G , as it would with enhancing the Kondo coupling J_K . These two quantities define a two-dimensional parameter space, which allows the consideration of a global phase diagram¹⁰. This global phase diagram is most clearly specified via the energy scale T^* associated with the breakdown of the Kondo entanglement between the local moments and conduction electrons. So far T^* has only been identified in tetragonal YbRh_2Si_2 (refs. ^{8,11,12}). It is believed that this energy scale not only provides a general characterization of the heavy fermion quantum criticality but also underlies the non-Fermi liquid behaviour and anomalous dynamical scaling¹²⁻¹⁴ observed in these and related materials.

In order to explore the additional axis of the global phase diagram, we take advantage of the fact that enhancing spatial dimensionality reduces the quantum fluctuation parameter G . Therefore, it would be invaluable to study the extreme three-dimensional cubic heavy fermion compounds and compare their quantum critical behaviour with that of the tetragonal and other non-cubic materials.

Here, we do so in the cubic heavy fermion compound $\text{Ce}_3\text{Pd}_{20}\text{Si}_6$. We show that this material undergoes a quantum phase transition at a readily accessible magnetic field, and are able to identify the Kondo breakdown energy scale T^* . This scale vanishes inside the ordered part of the compound’s phase diagram, thereby providing the first clear evidence for a Kondo breakdown in the three-dimensional part of the global phase diagram. Furthermore, we show that this vanishing scale is the origin of the non-Fermi liquid behaviour observed previously in this compound (Supplementary Information).

In the cubic crystal structure of space group $Fm\bar{3}m$, the Ce atoms occupy two different crystallographic sites, $4a$ (Ce1) and $8c$ (Ce2), both with cubic point symmetry¹⁵ (Fig. 1a). This structure persists down to at least 40 mK, as shown by high-resolution neutron diffraction measurements¹⁶. The magnetic susceptibility $\chi(T)$ is Curie-Weiss like above 100 K (Fig. 1b), with an effective moment close to the full moment ($2.54 \mu_B/\text{Ce}$) of the $J = 5/2$ spin-orbit ground state. A clear anomaly can be seen in $\chi(T)$ somewhat below T_N (Fig. 1c). The electrical resistivity $\rho(T)$ is typical of heavy fermion compounds. $\Delta\rho$, the resistivity with the phonon-scattering contribution subtracted, shows a $-\ln(T)$ behaviour due to incoherent Kondo scattering at high temperatures. The maximum at about 20 K signals the onset of Kondo screening (Fig. 1d). Also the Hall coefficient shows the typical heavy fermion behaviour at high temperatures (Fig. 1e). Between room temperature and 50 K it is well described by $R_H(T) = R_0 + R_A(T)$, where R_0 represents a temperature independent normal Hall coefficient and $R_A(T)$ an intrinsic skew-scattering term. At low temperatures, R_A becomes small and the measured Hall coefficient is dominated by the normal Hall component (Supplementary Information).

The specific heat $C(T)$ reveals that, in addition to the phase transition at T_N that is also seen in $\chi(T)$, there is a second phase transition at T_Q (Fig 1f, ref. ¹⁷). The upper transition at T_Q has been tentatively attributed to antiferro-quadrupolar order at the $8c$ site¹⁸, and the lower transition at T_N to magnetic order¹⁹ – presumably antiferromagnetic order in analogy with $\text{Ce}_3\text{Pd}_{20}\text{Ge}_6$ (ref. ²⁰). These assignments are consistent with the Γ_8 quartet and the Γ_7 doublet of the crystalline electric field split ground states of the Ce $4f$ orbitals on the $8c$ and $4a$ sites, respectively^{16,21}. The temperature–field phase diagram is shown in Fig. 1g. T_Q is initially enhanced by the applied field but is eventually reduced at larger fields. According to measurements on single crystals, magnetic field is able to completely suppress T_Q (ref. ¹⁹), suggesting the presence of a QCP at fields above 10 T. Within the ordered region $T_Q(B) > 0$,

T_N can be seen to decrease monotonically and vanish at about 0.9 T. This specifies a readily accessible QCP, thereby providing a rare opportunity to study quantum phase transitions in cubic heavy fermion materials.

It follows from general symmetry considerations that antiferro-quadrupolar ordering preserves the cubic symmetry of the lattice, as described in Supplementary Information. In addition, such considerations as well as microscopic calculations show that antiferro-quadrupolar order in the presence of magnetic field induces dipolar order, thereby influencing the antiferromagnetic correlations. The induced antiferromagnetic order, in turn, implies a magnetic-field tuning of the antiferro-quadrupolar transition temperature (Fig. S5 of Supplementary Information), which is compatible with the experimentally observed phase diagram (Fig. 1g). Through the magnetic coupling between the $8c$ and $4a$ sites, the entire ordered region will contain both magnetic and quadrupolar orders. Finally, in the absence of the competition by the RKKY interactions, the ground state multiplets at both sites will be quenched by their Kondo couplings with the conduction electrons.

Studying the isothermal control parameter dependence of transport properties is a well established means^{11,12} to probe the quantum critical fluctuations near a QCP. Fig. 2a-c shows selected isotherms of the Hall resistivity ρ_H as a function of the applied magnetic field B . At the lowest temperatures $\rho_H(B)$ shows two kinks (Fig. 2a). One of these persists as a broadened feature at temperatures above T_N (Fig. 2b,c). To quantify these features we fit the data with crossover functions (Methods), shown as lines in Fig. 2a-c. At temperatures above T_N , this procedure identifies the crossover field B^* , as well as the full width at half maximum FWHM and the step height $\Delta A = |A_1 - A_2|$ of the crossover. Below T_N , the fitting characterizes in addition the crossover at the Néel transition. The fitted quantities are shown in Fig. 3a-c for the crossover at B^* and in Fig. S3 of Supplementary Information for the crossover at B_N . Broadened kinks in $\rho_H(B)$ correspond to broadened steps in the differential Hall coefficient, defined as the field derivative of the Hall resistivity $d\rho_H/dB$. This is shown in Fig. 2d for the crossover at B^* .

The features in the Hall resistivity have their counterparts in the longitudinal and transverse magnetoresistance $\rho_l(B)$ and $\rho_t(B)$ (Fig. 2e,f). The B^* crossover appears as a broadened step-like decrease of the resistivity with increasing field. Below T_N , the B_N crossover is seen as an increase of the resistivity with field at small fields. The resistivity also contains a component that increases more gradually with field. This is identified as a background

contribution (Methods). The resistivity data with the background and the anomaly at T_N subtracted are shown in Fig. 2g,h and are fitted by the same crossover functions that describe the differential Hall coefficient. The fit parameters are also shown in Fig. 3a-c and Fig. S3 of Supplementary Information.

Fig. 3 demonstrates our key conclusions. $T^*(B)$ – which is equivalent to $B^*(T)$ – defines a crossover scale that is distinct from any phase transition line, except in the zero temperature limit where it merges with $T_N(B)$ at a common critical field of about 0.9 T (Fig. 3a). The $T^*(B)$ scale exists both outside and within the ordered part of the phase diagram delimited by the upper ordering temperature $T_Q(B)$. The FWHM of the crossover decreases with decreasing temperature, extrapolating to zero in the zero temperature limit as evidenced by the pure power-law behaviour of $\text{FWHM}(T)$ (Fig. 3b). At the same time the step height ΔA remains finite in the zero temperature limit (Fig. 3c). Because the Hall effect measures the response of the electronic excitations near the Fermi surface, the crossover at nonzero temperatures and the jump in the extrapolated zero-temperature limit are most naturally interpreted in terms of a collapse of the heavy fermion Fermi surface to a strongly reconstructed one. This implicates the T^* line as signifying a Kondo breakdown, which is tantamount to a localization of the f electrons.

The observation of the collapsing Kondo breakdown scale implies new quantum critical excitations which are neither of the Landau Fermi liquid nor of the spin density wave QCP type^{22,23}. Instead, electronic excitations over the entire Fermi surface are expected to have a non-Fermi liquid form²⁴⁻²⁶. In fact, the electrical resistivity is linear in T and the electronic specific heat coefficient $\Delta C(T)/T$ is logarithmic in T (refs.^{17,27}, Supplementary Information). Both are defining characteristics of non-Fermi liquid behaviour which appears also in other materials with Kondo breakdown QCPs. At magnetic fields away from $B^*(T = 0)$, a Fermi liquid T^2 temperature dependence of the electrical resistivity is recovered at low temperatures; measurements at several magnetic fields (up to 5 T) suggest that the corresponding temperature scale T_{FL} gradually decreases as B approaches $B^*(T = 0)$.

A collapsing Kondo breakdown scale has been observed in YbRh_2Si_2 (refs.^{8,11,12}). In that case the T^* line merges with the zero temperature boundary between paramagnetic and ordered phases, thereby signaling the destruction of the Kondo effect and concomitant reconstruction of the Fermi surface at the onset of magnetic order²⁴⁻²⁶. However, in $\text{Ce}_3\text{Pd}_{20}\text{Si}_6$ the T^* line enters an ordered phase at finite temperature. We interpret this distinction as

due to the different dimensionality of the two compounds.

Spatial dimensionality modifies the degree of fluctuations, including that of the quantum magnetism associated with the f moments. This is illustrated by the two-parameter global phase diagram shown in Fig. 4. The horizontal axis marks the strength J_K of the Kondo coupling between the local f moments and the conduction electrons. It controls the degree of quantum fluctuations due to spin flip processes associated with the Kondo coupling. The vertical axis G describes the degree of quantum fluctuations within the local moment component.

Going from the three-dimensional (3D) cubic limit to the decoupled 2D limit amounts to moving upwards along the vertical axis. The tetragonal structure of YbRh_2Si_2 suggests that it is close to the 2D limit, with enhanced G , making it natural to have the ordered to paramagnetic phase boundary coinciding with the Kondo collapse. The cubic structure of $\text{Ce}_3\text{Pd}_{20}\text{Si}_6$ implies a smaller G , placing it in the part of the global phase diagram where Kondo collapsing occurs inside the ordered part of the phase diagram. Here, the competition between the RKKY and Kondo couplings gives rise to a T^* line which separates two ordered ground states. Note that, at finite temperature, the T^* line is distinct from the ordering transition lines. In the zero-temperature limit, it separates a Kondo-screened order at $B > B^*$ and a Kondo-destroyed order at $B < B^*$. Through the field-induced mixing of the antiferro-quadrupolar and antiferromagnetic orderings (Sec. E of Supplementary Information), this corresponds to the region of the G - J_K phase diagram in Fig. 4 where a Kondo-destruction QCP (brown line) occurs within the ordered part of the phase diagram, from a phase AF_S to a phase AF_L .

Our results provide a way to think about other quantum critical heavy fermion metals, in line with recent theoretical considerations^{3,10,28,29}. CeIn_3 is another cubic system placing it in a similar part of the vertical axis as $\text{Ce}_3\text{Pd}_{20}\text{Si}_6$. There is some indication for the divergence of the effective quasiparticle mass inside the ordered part of its phase diagram³⁰ making it instructive to search for the T^* scale in that system. The recently designed $\text{CeIn}_3/\text{LaIn}_3$ superlattice³¹ amounts to an elegant reduction of the dimensionality towards the extreme 2D limit. Resistivity measurements have already provided evidence for a reduced strength of magnetic ordering. It will also be illuminating to explore the possibility of a Kondo breakdown. Finally, there are materials which have 2D lattices that host geometrical frustration such as the Shastry-Sutherland lattice in $\text{Ce}_2\text{Pt}_2\text{Pb}$ (ref. ³²). It is possible that

these materials have even higher G making them promising candidates to shed light on the upper part of the global phase diagram.

Reconstruction of Fermi surface is also being extensively discussed in other electronic materials, including cuprate superconductors³³. Typically, it is tied to antiferromagnetic ordering or other spontaneous symmetry breaking transitions. Here, in $\text{Ce}_3\text{Pd}_{20}\text{Si}_6$, we find Fermi-surface reconstructions both at the antiferromagnetic transition, the T_N line, and away from it, at the T^* line. While the former is smooth, the latter extrapolates to a jump of the Fermi surface in the zero-temperature limit. Our results amount to a rare demonstration of Fermi-surface reconstruction away from symmetry-breaking transitions. By extension, our findings highlight the emergence of novel electronic excitations through a mechanism other than spontaneous symmetry breaking, a notion that is of considerable current interest in a variety of settings including topological matters.

To summarize, we have observed an energy scale associated with the destruction of the Kondo effect and the concomitant f -electron localization in a cubic heavy fermion compound. This not only extends the materials basis for this effect to the 3D extreme but also unambiguously establishes that the origin of the T^* scale lies in robust many body correlations, as opposed to materials specific band structure effects. Our findings suggest a materials based global phase diagram for heavy fermion systems, which not only highlights a rich variety of quantum critical points but also indicates an underlying universality. Given that quantum critical fluctuations represent an established route towards unconventional superconductivity, the insight we have gained will likely be important for the physics of high-temperature superconductors.

Methods

Synthesis and sample selection. The polycrystalline samples were prepared from high-purity elements (Ce 99.99%, Pd 99.998%, Si 99.9999%) by either ultra-high purity argon-arc or radio-frequency heating. Because of the excellent stoichiometry of these polycrystals they are of higher quality than the best available single crystals; this is evidenced by larger residual resistance ratios, sharper phase transition anomalies and higher transition temperatures in the polycrystals^{18,19,34}. The phase transition temperature $T_N(B)$ is isotropic in field down to the lowest measured temperature¹⁹. We therefore chose these polycrystals for our investigation.

Characterization. The magnetotransport measurements were performed by a standard

4-point ac technique in an Oxford dilution refrigerator and, above 2 K, in a PPMS from Quantum Design. The magnetization measurements were performed by a capacitive technique at low temperatures and in a SQUID magnetometer of Cryogenic Ltd. above 2 K.

Data analysis. The crossover in the magnetoresistance at B^* was fitted with the empirical crossover function

$$\rho(B) = A_2 - \frac{A_2 - A_1}{1 + (B/B^*)^p} \quad (1)$$

introduced in ref.¹¹, and the crossover at T_N with the function

$$\rho(B) = A_2 - \frac{A_2 - A_1}{1 + e^{\frac{B-B_N}{w}}}. \quad (2)$$

The latter function was chosen because it represents a single, symmetrically broadened step of height ΔA and width w at the finite field B_N , that describes the data very well. The Hall resistivity was modeled with the integral over these fitting functions.

As discussed in the main text, a smooth overall increase of ρ with only weak temperature dependence appears to be superimposed onto these two features. Measuring the magnetoresistance in both the longitudinal (field parallel to electrical current, Fig. 2e) and the transverse (field perpendicular to electrical current, Fig. 2f) configuration helps us to identify this latter as a background contribution due to normal magnetoresistance. It is featureless at the QCP and should be eliminated for the analysis of quantum criticality. We approximate the temperature dependent background by rescaling the background functions of the lowest temperature isotherms (grey lines in Fig. 2e,f) with the quadratic temperature dependence of the 15 T resistivity data observed at the lowest temperatures. After the subtraction of this background ($\rho_{l,\text{back}}$ and $\rho_{t,\text{back}}$) the crossover-related magnetoresistance approaches zero at high fields. An exemplary fit is shown in Fig. S2 of Supplementary Information.

References

1. Friedemann, S. *et al.* Detaching the antiferromagnetic quantum critical point from the Fermi-surface reconstruction in YbRh_2Si_2 . *Nature Phys.* **5**, 465–469 (2009).
2. Tokiwa, Y., Gegenwart, P., Geibel, C. & Steglich, F. Separation of energy scales in undoped YbRh_2Si_2 under hydrostatic pressure. *J. Phys. Soc. Jpn.* **78**, 123708 (2009).
3. Custers, J. *et al.* Evidence for a non-Fermi-liquid phase in Ge-substituted YbRh_2Si_2 . *Phys. Rev. Lett.* **104**, 186402 (2010).
4. Schofield, A. J. Quantum criticality and novel phases: Summary and outlook. *Phys. Status Solidi B* **247**, 563–569 (2010).
5. Broun, D. M. What lies beneath the dome? *Nature Phys.* **4**, 170–172 (2008).
6. v. Löhneysen, H. *et al.* Non-Fermi-liquid behavior in a heavy-fermion alloy at a magnetic instability. *Phys. Rev. Lett.* **72**, 3262–3265 (1994).
7. Mathur, N. *et al.* Magnetically mediated superconductivity in heavy fermion compounds. *Nature* **394**, 39–43 (1998).
8. Gegenwart, P. *et al.* Multiple energy scales at a quantum critical point. *Science* **315**, 969–971 (2007).
9. Park, T. *et al.* Hidden magnetism and quantum criticality in the heavy fermion superconductor CeRhIn_5 . *Nature* **440**, 65–68 (2006).
10. Si, Q. Global magnetic phase diagram and local quantum criticality in heavy fermion metals. *Physica B* **378–380**, 23–27 (2006).
11. Paschen, S. *et al.* Hall-effect evolution across a heavy-fermion quantum critical point. *Nature* **432**, 881–885 (2004).
12. Friedemann, S. *et al.* Fermi-surface collapse and dynamical scaling near a quantum-critical point. *PNAS* **107**, 14547–14551 (2010).
13. Aronson, M. *et al.* Non-Fermi-liquid scaling of the magnetic response in $\text{UCu}_{5-x}\text{Pd}_x$ ($x = 1, 1.5$). *Phys. Rev. Lett.* **75**, 725–728 (1995).
14. Schröder, A. *et al.* Onset of antiferromagnetism in heavy-fermion metals. *Nature* **407**, 351–355 (2000).
15. Griбанov, A. V., Seropegin, Y. D. & Bodak, O. I. Crystal structure of the compounds

- Ce₃Pd₂₀Ge₆ and Ce₃Pd₂₀Si₆. *J. Alloys Compd.* **204**, L9–L11 (1994).
16. Deen, P. P. *et al.* Quantum fluctuations and the magnetic ground state of Ce₃Pd₂₀Si₆. *Phys. Rev. B* **81**, 064427 (2010).
 17. Strydom, A. M., Pikul, A., Steglich, F. & Paschen, S. Possible field-induced quantum criticality in Ce₃Pd₂₀Si₆. *J. Phys.: Conf. Series* **51**, 239–242 (2006).
 18. Goto, T. *et al.* Quadrupole ordering in clathrate compound Ce₃Pd₂₀Si₆. *J. Phys. Soc. Jpn.* **78**, 024716 (2009).
 19. Mitamura, H. *et al.* Low temperature magnetic properties of Ce₃Pd₂₀Si₆. *J. Phys. Soc. Jpn.* **79**, 074712 (2010).
 20. Dönni, A. *et al.* Low-temperature antiferromagnetic moments at the 4a site in Ce₃Pd₂₀Ge₆. *J. Phys.: Condens. Matter* **12**, 9441–9451 (2000).
 21. Paschen, S. *et al.* First neutron measurements on Ce₃Pd₂₀Si₆. *Physica B* **403**, 1306–1308 (2008).
 22. Hertz, J. Quantum critical phenomena. *Phys. Rev. B* **14**, 1165–1184 (1976).
 23. Millis, A. J. Effect of a nonzero temperature on quantum critical points in itinerant fermion systems. *Phys. Rev. B* **48**, 7183–7196 (1993).
 24. Si, Q., Rabello, S., Ingersent, K. & Smith, J. Locally critical quantum phase transitions in strongly correlated metals. *Nature* **413**, 804 (2001).
 25. Coleman, P., Pépin, C., Si, Q. & Ramazashvili, R. How do Fermi liquids get heavy and die? *J. Phys.: Condens. Matter* **13**, R723 (2001).
 26. Senthil, T., Vojta, M. & Sachdev, S. Weak magnetism and non-Fermi liquids near heavy-fermion critical points. *Phys. Rev. B* **69**, 035111 (2004).
 27. Paschen, S. *et al.* Quantum critical behaviour in Ce₃Pd₂₀Si₆? *J. Magn. Magn. Mater.* **316**, 90–92 (2007).
 28. Si, Q. Global magnetic phase diagram and local quantum criticality in heavy fermion metals. *Phys. Status Solidi* **247**, 476–484 (2010).
 29. Coleman, P. & Nevidomskyy, A. Frustration and the Kondo effect in heavy fermion materials. *J. Low Temp. Phys.* **161**, 182–202 (2010).
 30. Sebastian, S. E. *et al.* Heavy holes as a precursor to superconductivity in antiferromagnetic CeIn₃. *PNAS* **106**, 7741–7744 (2009).
 31. Shishido, H. *et al.* Tuning the dimensionality of the heavy fermion compound CeIn₃. *Science*

- 327**, 980–983 (2010).
32. Kim, M. S. & Aronson, M. C. Heavy fermion compounds on the geometrically frustrated Shastry-Sutherland lattice. *J. Phys.: Condens. Matter* **23**, 164204 (2011).
 33. Helm, T. *et al.* Evolution of the Fermi surface of the electron-doped high-temperature superconductor $\text{Nd}_{2-x}\text{Ce}_x\text{CuO}_4$ revealed by Shubnikov–de Haas oscillations. *Phys. Rev. Lett.* **103**, 157002 (2009).
 34. Prokofiev, A. *et al.* Crystal growth and composition-property relationship of $\text{Ce}_3\text{Pd}_{20}\text{Si}_6$ single crystals. *Phys. Rev. B* **80**, 235107 (2009).

Acknowledgements

The authors wish to thank S. Kirchner for useful discussions. The work was funded by the European Research Council under the European Community’s Seventh Framework Programme (FP7/2007-2013)/ERC grant agreement no. 227378 and by the Austrian Science Foundation (project P19458-N16). A.St. thanks the SA-NRF (2072956) and the URC of the University of Johannesburg for financial assistance. R.Y. and Q.S. acknowledge the support of NSF Grant No. DMR-1006985 and the Robert A. Welch Foundation Grant No. C-1411.

Author contributions

S.P. initiated the study. S.P. and Q.S. designed the research. A.St. and A.P. synthesized and characterized the material. J.C., K.L., M.M., and H.W. performed magnetotransport measurements, A.Si. and Y.S. magnetization measurements. T.S. led the low-temperature magnetization investigation. K.L., H.W., A.Si., and S.P. analyzed the data. R.Y. and Q.S. set up the theoretical framework and performed the calculations. S.P., Q.S., and R.Y. prepared the manuscript. All authors contributed to the discussion.

Additional Information

The authors declare that they have no competing financial interests. Supplementary information accompanies this paper on www.nature.com/naturematerials. Reprints and permission information is available online at <http://www.nature.com/reprints>. Correspondence and requests for materials should be addressed to S.P.

FIG. 1: Characteristics of the heavy fermion compound $\text{Ce}_3\text{Pd}_{20}\text{Si}_6$. **a**, Cubic crystal structure. **b**, Inverse volume susceptibility in SI units $1/\chi^{\text{SI}}$ in the linear response regime vs temperature T . A Curie-Weiss fit at high temperatures yields an effective moment $\mu = 2.35\mu_{\text{B}}$ per Ce atom and a paramagnetic Weiss temperature $\Theta = -3$ K. **c**, A maximum in $\chi^{\text{SI}}(T)$ somewhat below T_{N} clearly reveals the Néel transition. Only a very weak feature can be discerned at the putative antiferro-quadrupolar transition at T_{Q} . **d**, Temperature-dependent electrical resistivity $\rho(T)$ and $\Delta\rho(T) = \rho(T) - \rho_{\text{ph}}(T)$, where the contribution due to phonon scattering $\rho_{\text{ph}}(T)$ is determined from the non- f reference compound $\text{La}_3\text{Pd}_{20}\text{Si}_6$ as in ref.¹⁷. **e**, Temperature dependent Hall coefficient in the linear response regime $R_{\text{H}}(T)$, together with a fit according to the anomalous Hall effect model described in Supplementary Information, and its extrapolation to lower temperatures (dashed line). The normal Hall coefficient R_0 , assumed as temperature independent in this model, is shown as grey line. **f**, Electronic contribution to the specific heat ΔC vs T in an applied magnetic field of 0.5 T (from ref.¹⁷). The two anomalies at T_{N} and T_{Q} are clear signatures of second-order phase transitions. It is expected that their ordering wavevectors are different. As in ref.²⁷ the transition temperatures are estimated by entropy balance constructions. **g**, Temperature-field phase diagram with the transition temperatures T_{N} and T_{Q} , determined from transport and specific heat measurements, respectively.

FIG. 2: Magnetotransport across the quantum critical point of $\text{Ce}_3\text{Pd}_{20}\text{Si}_6$. **a**, Hall resistivity ρ_H vs applied magnetic field B at different temperatures below T_N . The solid lines represent fits of a crossover function (see Methods) to the data. **b**, **c**, Corresponding plots for intermediate and high temperatures. The crossover fields B_N and B^* of the fits are indicated in **a-c**. **d**, Field derivative of the fits of **a-c**, $d\rho_H/dB$, normalized to the step height ΔA , vs normalized field B/B^* . The extrapolated zero-temperature form, a sharp step, is shown as grey line. **e**, Longitudinal magnetoresistance ρ_l vs B at different temperatures (80, 100, 125, 150, 175, 200, 250, 301, 350, 402, 500, 602, 700, 900 mK, 1.1, 1.3, 1.5, 1.7, 1.9, 2.9, 5.0 K). **f**, Corresponding plot for transverse magnetoresistance ρ_t (89, 193, 300, 366, 486, 632, 743, 963 mK, 1.1, 1.3, 1.5, 1.7, 2.0, 3.0, 5.0 K). The grey curves in **e** and **f** represent the background (see Methods). **g**, Crossover component at B^* (see Methods) of $\rho_l(B)$, normalized to the zero-field resistivity at the respective temperature, vs normalized field B/B^* . The data points are shown as dots, the fits as full lines. The grey line again represents the extrapolated zero-temperature form. **h**, Corresponding plot for $\rho_t(B)$.

FIG. 3: Characteristics of the Fermi surface collapse in $\text{Ce}_3\text{Pd}_{20}\text{Si}_6$. **a**, Temperature $T^*(B)$ of the crossover at $B^*(T)$, determined from the fits of $\rho_H(B)$, $\rho_l(B)$, and $\rho_t(B)$ in Fig. 2, plotted in the temperature-field phase diagram of Fig. 1g. **b**, Temperature dependence of the full width at half maximum, $\text{FWHM}(T)$, of the crossover. **c**, Temperature dependence of the step height, $\Delta A(T)$, of the crossover. The crosses refer to Hall resistivity data corrected for the anomalous Hall effect (Supplementary Information).

FIG. 4: Materials-based global phase diagram for heavy fermion compounds near antiferromagnetic instabilities. Magnetic frustration parameter G (left) vs Kondo coupling J_K at $T = 0$. Lines of quantum critical points separate antiferromagnetic (AF) from paramagnetic (P) regions (thick red line), and regions of small (S) and large (L) Fermi surface (brown line). The latter line represents quantum critical points accompanied by a Kondo breakdown. Dimensionality (right) helps to calibrate the placement of selected materials (CPS: $\text{Ce}_3\text{Pd}_{20}\text{Si}_6$, CeIn_3 , a $\text{CeIn}_3/\text{LaIn}_3$ superlattice, YRS: YbRh_2Si_2 , CCA: $\text{CeCu}_{6-x}\text{Au}_x$, CPP: $\text{Ce}_2\text{Pt}_2\text{Pb}$, marked on the G -axis by the ticks) along the vertical axis. The present work allows to elucidate the three-dimensional part of the phase diagram.

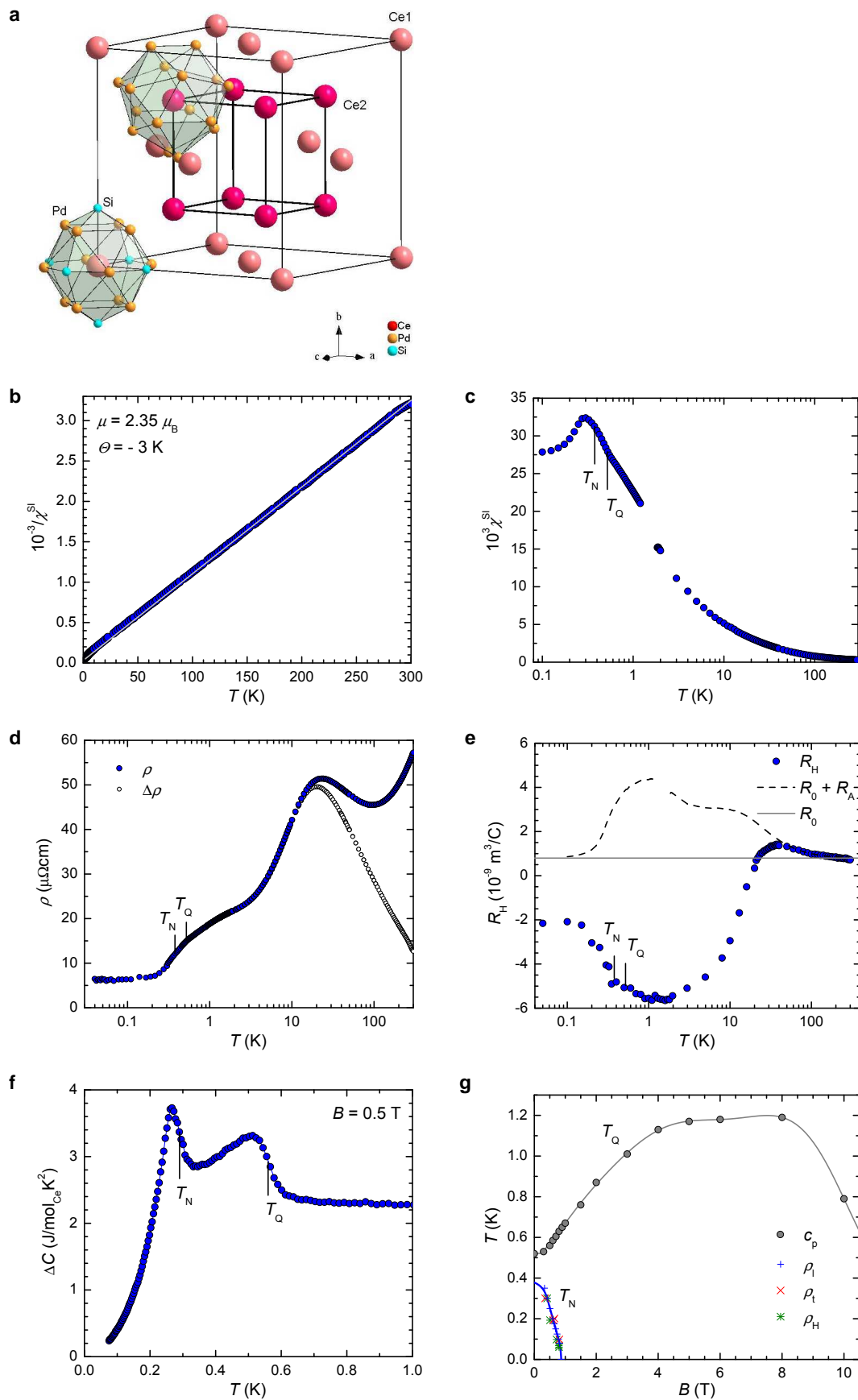


Figure 1

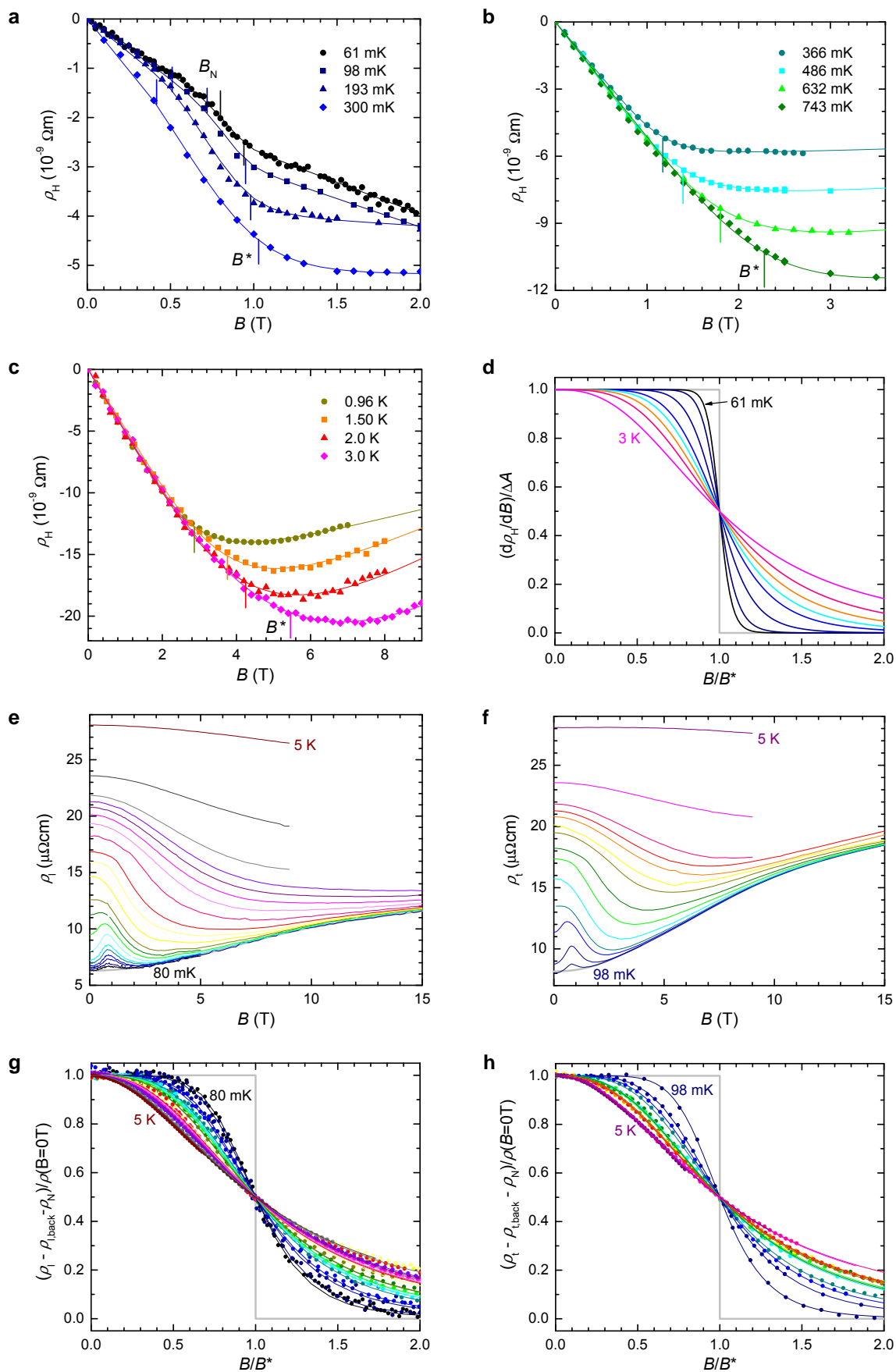


Figure 2

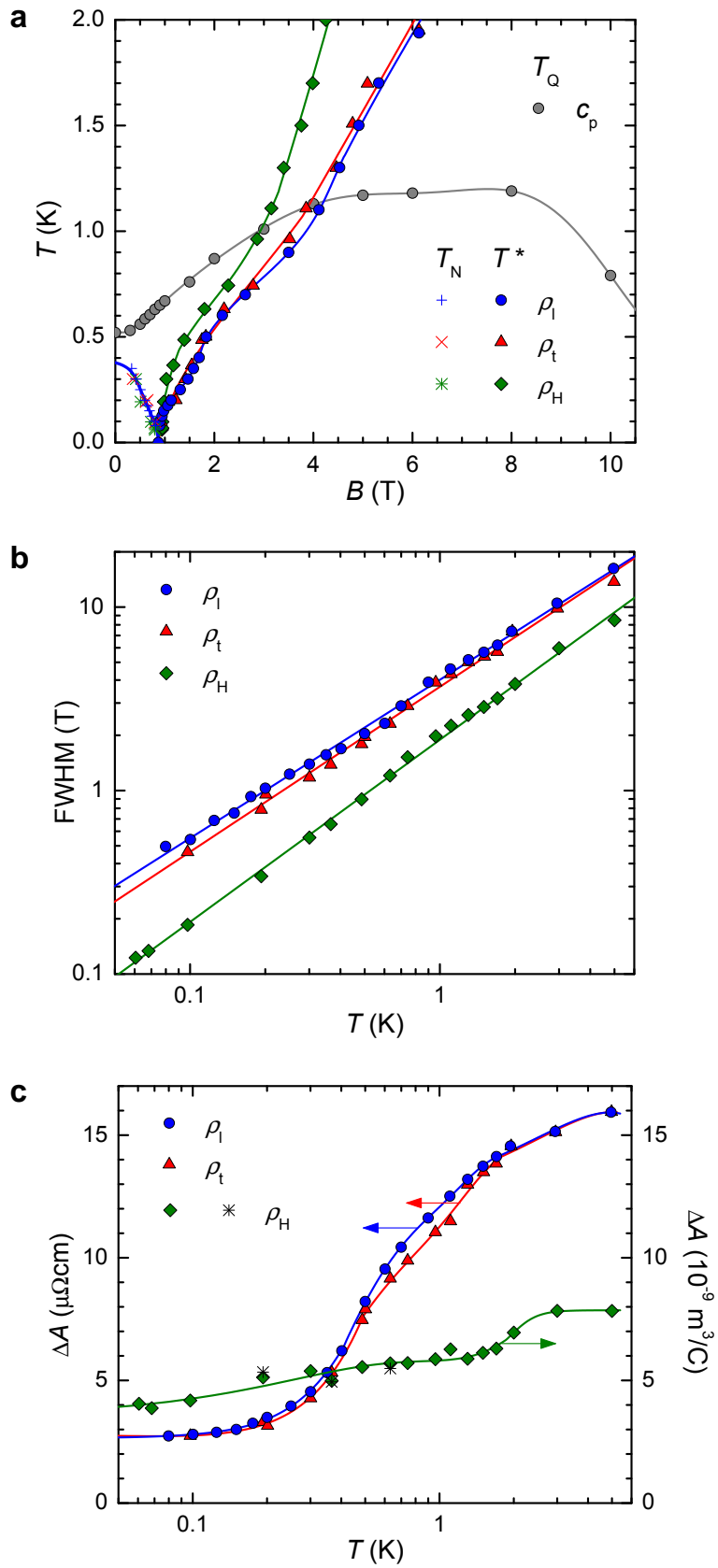


Figure 3

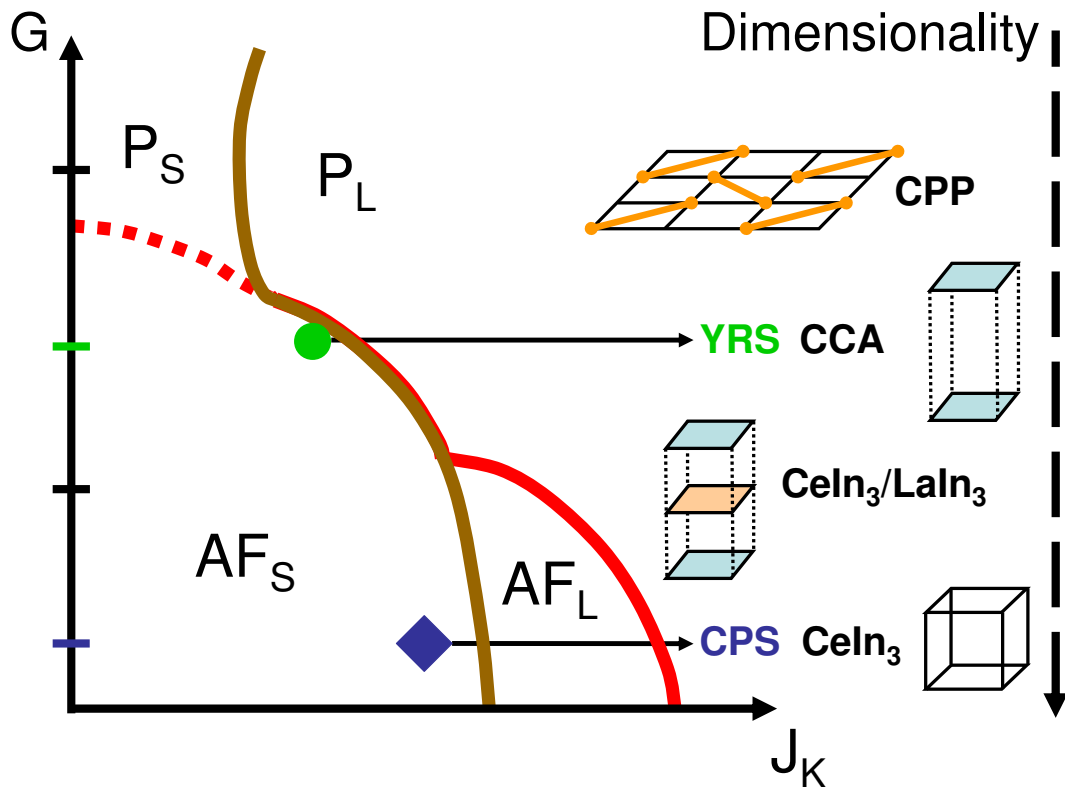


Figure 4

Destruction of Kondo effect in cubic heavy fermion compound $\text{Ce}_3\text{Pd}_{20}\text{Si}_6$: Supplementary Information

J. Custers¹, K.-A. Lorenzer¹, M. Müller¹, A. Prokofiev¹, A. Sidorenko¹, H. Winkler¹, A. M. Strydom², Y. Shimura³, T. Sakakibara³, R. Yu⁴, Q. Si⁴, and S. Paschen^{1*}

¹ Institute of Solid State Physics, Vienna University of Technology, 1040 Vienna, Austria

² Physics Department, University of Johannesburg, Auckland Park 2006, South Africa

³ Institute for Solid State Physics, University of Tokyo, Kashiwa 277-8581, Japan

⁴ Department of Physics and Astronomy, Rice University, Houston, TX 77005, USA

* e-mail: paschen@ifp.tuwien.ac.at

A. Non-Fermi liquid properties

Non-Fermi liquid behaviour is observed in $\text{Ce}_3\text{Pd}_{20}\text{Si}_6$, as has been reported previously^{1,2}. At a field of 1 T, close to the critical field of 0.9 T, the low-temperature electrical resistivity is linear in T (Fig. S1a, ref. ¹) and the electronic specific heat coefficient $\Delta C(T)/T$ is logarithmic in T (Fig. S1b, ref. ²). This is to be contrasted with the behaviour expected at a 3D spin density wave QCP, namely a $T^{3/2}$ temperature dependence for the electrical resistivity and $A - B\sqrt{T}$ for $\Delta C(T)/T$. At fields further away from the critical field, Landau Fermi liquid behaviour is recovered at lowest temperatures as clearly seen in the form of a T^2 dependence of the electrical resistivity. At higher temperatures, however, non-Fermi liquid characteristics are observed for a broader field range indicating that a fan of quantum critical behaviour emanates from the QCP with increasing temperature and extends even to above T_Q . Note the very large value of the electronic specific heat coefficient that reaches more than $7 \text{ J/mol}_{\text{Ce}}\text{K}^2$ in the non-Fermi liquid region.

B. Fitting the crossover data

The magnetoresistivity with crossovers at B^* and B_N was analyzed with the sum of two empirical fitting functions (equations (1) and (2), Methods). Figure S2 shows a typical result for the longitudinal magnetoresistivity, with the background contribution subtracted. The grey line is the sum of the two functions. It describes the data very well. Above the Néel temperature, only the crossover at B^* remains and thus the data were fit to equation (1).

C. Crossover at the Néel transition

The fit parameters characterizing the crossover at B^* were given in Fig. 3 of the main part. In Fig. S3 we show the corresponding quantities for the crossover at the Néel transition.

Both the step height ΔA_N and the crossover width w_N increase with decreasing temperature. This is in contrast to the crossover at B^* which becomes infinitely sharp in the extrapolated zero temperature limit.

D. Anomalous Hall effect

As is typical for heavy fermion metals the temperature dependence of the Hall coefficient R_H at high temperatures is dominated by an anomalous Hall component due to intrinsic skew-scattering, $R_A(T) = \gamma\rho_{\text{mag}}(T)\chi(T)$, where $\rho_{\text{mag}}(T) = \rho(T) - \rho_{\text{ph}}(T) - \rho_0$ is the intrinsic magnetic contribution to the electrical resistivity $\rho(T)$, $\rho_{\text{ph}}(T)$ is the phonon contribution determined via the non-magnetic reference compound $\text{La}_3\text{Pd}_{20}\text{Si}_6$, ρ_0 is the residual resistivity, $\chi(T)$ is the magnetic susceptibility, and γ is a positive constant³. This was shown in Fig. 1e of the main part where, in the incoherent Kondo regime above 50 K, the measured $R_H(T)$ is well described by the sum of a temperature independent normal Hall coefficient R_0 and $R_A(T)$. The constant $\gamma = (1.29 \pm 0.03) \text{ m}^2/\text{Vs}$ was determined by plotting R_H vs $\rho_{\text{mag}}\chi$, with temperature as implicit parameter, which varies approximately linearly between room temperature and 50 K (not shown). The $R_0 + R_A$ curve below 50 K was determined by assuming, as in refs.^{4,5}, that γ remains temperature independent down to the lowest temperatures. As seen in Fig. 1e of the main part, $R_A(T)$ remains positive and becomes negligibly small at the lowest temperatures. The measured Hall coefficient, on the other hand, becomes negative below about 20 K and saturates at the lowest temperatures. It must, therefore, be dominated by a temperature dependent normal Hall component.

In addition to the intrinsic skew-scattering term, there is an extrinsic contribution due to skew-scattering defects that might become relevant at the lowest temperatures. In order to estimate its magnitude we assume that, as an upper boundary, the entire difference of the residual resistivities of $\text{Ce}_3\text{Pd}_{20}\text{Si}_6$ and $\text{La}_3\text{Pd}_{20}\text{Si}_6$, about 10% of ρ_0 , is skew-scattering active. The extrinsic anomalous Hall effect then amounts to 10% of R_H at the lowest accessed temperature.

Finally, we clarify whether the magnetic field dependence of the measured Hall resistivity $\rho_H(B)$ is perturbed by an anomalous contribution $\rho_H^{\text{a}}(B) = \gamma\rho_{\text{skew}}(B)\mu_0M(B)$. $\rho_{\text{skew}}(B)$ contains the temperature and field dependent background contribution to the longitudinal resistivity $\rho_{\text{l,back}}$ (see Methods) and the above discussed 10% of ρ_0 . In Fig. S4 the normal component to the Hall resistivity $\rho_H^0(B) = \rho_H(B) - \rho_H^{\text{a}}$ is shown at three selected temperatures, together with the ρ_H data and their fits. ρ_H^{a} reaches at maximum 20% of ρ_H .

Interestingly, $\rho_{\text{H}}^0(B)$ is very well described by crossover functions that differ from the fits of $\rho_{\text{H}}(B)$ only by slightly different crossover heights ΔA . These are included as stars in Fig. 3c of the main part and Fig. S3a. Thus, taking the anomalous Hall effect into account has no significant effect on the outcome of our analyses.

E. Antiferromagnetic order induced by antiferro-quadrupolar order: microscopic and symmetry-based analyses

In $\text{Ce}_3\text{Pd}_{20}\text{Si}_6$, the Ce^{3+} ion has one localized f electron with angular momentum $J = 5/2$. In cubic environment, the six-fold degenerate ground-state multiplet is further split into a Γ_8 quartet and a Γ_7 doublet. We will take the experimentally suggested⁶ ground state of the Ce ion, which is a Γ_7 doublet for the $4a$ site and a Γ_8 quartet for the $8c$ site. Building upon the suggestion of ultrasound measurements⁷, we associate the high-temperature transition at T_{Q} with antiferro-quadrupolar (AFQ) order of the Γ_8 subsystem of Ce ions on the $8c$ site.

In this section, we show that, in the presence of a magnetic field, the AFQ order is expected to induce antiferromagnetic (AFM) order. This is seen through both a microscopic analysis of an effective pseudospin model, as well as a symmetry-based analysis of a Ginzburg-Landau functional. We also demonstrate that the AFQ order preserves the cubic structural symmetry, and that the experimentally observed evolution of the AFQ order as a function of the magnetic field is compatible with both the microscopic model calculation and symmetry-based considerations.

Effective pseudospin model

We will concentrate on the Ce ions of the $8c$ site, which form a simple cubic sublattice. The Γ_8 quartet can be described through two pseudospin operators⁸, $\boldsymbol{\sigma}$ and $\boldsymbol{\tau}$, which respectively act on the Kramers and non-Kramers doublet states. We can then express the RKKY coupling in terms of these pseudospin operators in a Kugel-Khomskii way^{9,10}:

$$\mathcal{H} = J \sum_{\langle i,j \rangle} [\boldsymbol{\tau}_i \cdot \boldsymbol{\tau}_j + \boldsymbol{\sigma}_i \cdot \boldsymbol{\sigma}_j + 4(\boldsymbol{\tau}_i \cdot \boldsymbol{\tau}_j)(\boldsymbol{\sigma}_i \cdot \boldsymbol{\sigma}_j)] + \mathcal{H}_Z, \quad (1)$$

where J is the nearest neighbor coupling strength, and \mathcal{H}_Z is the Zeeman term associated with the applied magnetic field $\mathbf{H} = (H_x, H_y, H_z)$.

The Γ_8 system comprises three dipoles, five quadrupoles and seven octupoles, all of which are irreducible representations of the O_h group of the cubic lattice. We denote them by $\boldsymbol{\tau}'$,

$\boldsymbol{\mu}$, $\boldsymbol{\sigma}$, $\boldsymbol{\eta}$, $\boldsymbol{\zeta}$, and ξ (defined in terms of $\boldsymbol{\tau}$ and $\boldsymbol{\sigma}$, Table I), and rewrite equation (1) as

$$\mathcal{H} = \sum_{\langle i,j \rangle} [J_\tau \boldsymbol{\tau}'_i \cdot \boldsymbol{\tau}'_j + J_\mu \boldsymbol{\mu}_i \cdot \boldsymbol{\mu}_j + J_\sigma \boldsymbol{\sigma}_i \cdot \boldsymbol{\sigma}_j + J_\eta \boldsymbol{\eta}_i \cdot \boldsymbol{\eta}_j + J_\zeta \boldsymbol{\zeta}_i \cdot \boldsymbol{\zeta}_j + J_\xi \xi_i \cdot \xi_j] + \mathcal{H}_Z. \quad (2)$$

Here, the first two terms refer to quadrupole-quadrupole interactions; the third and fourth terms are couplings among both the dipoles and octupoles; the next two terms are purely among the octupoles. By allowing the couplings to take different values in equation (2), we have extended equation (1) to a more general (and realistic) microscopic Hamiltonian that is compatible with the cubic lattice symmetry. The different coupling values also lift the degeneracy among the different types of multipoles. In order to stabilize the AFQ order, we take the first two couplings to be positive; through equation (1) the remaining couplings will also be taken as positive. The ultrasound experiment⁷ has been interpreted in terms of an AFQ phase with an ordering wavevector (π, π, π) , although it is also compatible with a (q, q, q) AFQ order (and its symmetry equivalents) for any nonzero q . The Zeeman term \mathcal{H}_Z reads $\mathcal{H}_Z = -\frac{7}{3}g\mu_B \sum_i (\boldsymbol{\sigma}_i + \frac{4}{7}\boldsymbol{\eta}_i) \cdot \mathbf{H}$, where $g = 6/7$ is the appropriate gyromagnetic factor.

The quadrupolar moments may couple to elastic strain via⁷ $\mathcal{H}_{QS} = -\sum_{i,\delta} g_\delta O_\delta(i) \varepsilon_\delta$, where $\delta = x^2 - y^2, 2z^2 - x^2 - y^2, xy, xz, yz$, ε_δ refers to the elastic strain of the δ 's component, and g_δ is the corresponding coupling constant. Through this coupling to elastic distortion, quadrupolar order may spontaneously break the cubic lattice symmetry. This is the case in the $\text{Ce}_3\text{Pd}_{20}\text{Ge}_6$ system^{11,12}, where the ferroquadrupolar order reduces the lattice symmetry from cubic to tetragonal. However, in our model for $\text{Ce}_3\text{Pd}_{20}\text{Si}_6$ the (π, π, π) AFQ order has a zero net quadrupolar moment, which could not directly couple to elastic distortion. In other words, the AFQ order preserves the cubic symmetry. We will therefore retain the cubic lattice symmetry in the remainder of the analysis.

Microscopic studies of the AFQ and AFM orders of the effective pseudospin model

In order to address the coupling between the AFQ and AFM orders in the presence of a magnetic field, as well as the field evolution of T_Q , we solve the model Hamiltonian of equation (2) at the mean-field level. For each pair of pseudospin operators $\boldsymbol{\phi}_i \cdot \boldsymbol{\phi}_j$ (where $\boldsymbol{\phi} = \boldsymbol{\tau}', \boldsymbol{\mu}, \boldsymbol{\sigma}, \boldsymbol{\eta}, \boldsymbol{\zeta}, \xi$) we perform a mean-field decomposition $\boldsymbol{\phi}_i \cdot \boldsymbol{\phi}_j \approx \langle \boldsymbol{\phi}_i \rangle \cdot \boldsymbol{\phi}_j + \boldsymbol{\phi}_i \cdot \langle \boldsymbol{\phi}_j \rangle - \langle \boldsymbol{\phi}_i \rangle \cdot \langle \boldsymbol{\phi}_j \rangle$. We assume a two-sublattice AFQ order with ordering vector (π, π, π) [or (q, q, q)], introduce the uniform and staggered components of the mean-field parameters as $\boldsymbol{\phi}_f = (\langle \boldsymbol{\phi}_A \rangle + \langle \boldsymbol{\phi}_B \rangle)/2$ and $\boldsymbol{\phi}_a = (\langle \boldsymbol{\phi}_A \rangle - \langle \boldsymbol{\phi}_B \rangle)/2$ for the sublattices A and B, and minimize

the free energy.

As suggested by ultrasound measurements⁷, the coupling strength between Γ_5^+ quadrupolar moments is stronger than the one between Γ_3^+ moments. To reflect this in the model, we set $J_\tau = 1$, and take $J_\mu > J_\tau$. Since we are mainly interested in the ordering of quadrupolar and dipolar moments, we reduce the coupling strengths of the pure octupolar moments by hand. Without loss of generality, we will work with the following parameters: $J_\tau = 1$, $J_\mu = 1.1$, $J_\sigma = J_\eta = 1$, and $J_\zeta = J_\xi = 0.75$.

We study the finite-temperature magnetic phase diagram in the presence of an external magnetic field. The direction of the magnetic field can be expressed by two angles θ and ϕ with $H_x = H \sin \theta \cos \phi$, $H_y = H \sin \theta \sin \phi$, and $H_z = H \cos \theta$. In Fig. S5 we present the phase diagrams for two field directions: (a) $\theta = \phi = 0$, *i.e.*, the field along the $[0,0,1]$ axis; (b) $\theta = \phi = \pi/4$, which corresponds to a generic direction (as opposed to high symmetry directions). At zero field, there is a continuous phase transition from the paramagnetic to an AFQ ordered phase at $T_Q \approx 0.28J_\tau$, but no magnetic dipolar order is found down to zero temperature. When applying a magnetic field, along both directions T_Q first rises up with increasing magnetic field, and the AFQ phase is stable in a broad field range. At elevated fields, the phase diagram shows strong anisotropy. The AFQ phase is more stable for the field direction $\theta = \phi = \pi/4$ where it survives up to a higher temperature ($T \approx 0.47J_\tau$), and to a higher magnetic field ($H \approx 5.2J_\tau$). The dominant AFQ moment is also different along the two directions. For $\theta = \phi = 0$, a Γ_3 -type (O_2^0) AFQ order is stabilized at intermediate fields, while the Γ_5 -type order is stabilized at either low or high fields. The regimes with different quadrupolar orders are separated by first-order transitions. Along the $\theta = \phi = \pi/4$ direction, the Γ_3 - and Γ_5 -type orders can coexist, but the dominant order parameter shows a crossover from $O_{xz} + O_{yz}$ in low fields to O_2^0 in high fields.

At zero magnetic field, the quadrupolar moments and the dipolar moments transform according to different irreducible representations of the cubic group. Therefore, no magnetic dipolar moment can be induced by the ordered quadrupolar moment. A nonzero magnetic field reduces the cubic symmetry of the electronic degrees of freedom, and the ordered AFQ moments may induce magnetic dipolar moments with the same point group symmetry and same ordering wavevector. For instance, the O_2^0 -type AFQ order induces AFM moment J^z under a magnetic field along the $[0,0,1]$ direction. Though there is no spontaneous magnetic order, the induced AFM order will make part of or even the entire AFQ phase magnetically

active depending on the symmetry of the AFQ moments. These parts are shown as the shaded areas in Fig. S5.

For a single crystalline sample in a magnetic field along a crystallographic high symmetry direction, the AFQ ordered phase may not be entirely magnetically ordered, as shown in the left panel of Fig. S5. However, the situation is different for a polycrystalline sample. There, one has to average over all the possible angles between the crystalline axes and the field. For any generic field orientation, the AFQ ordering always induce magnetic order, as exemplified by the right panel of Fig. S5. Therefore, for a polycrystalline sample, the entire AFQ ordered phase will be AFM ordered. By extension, such a material will not display any features associated with first order transitions between AFQ orders.

Ginzburg-Landau analysis

Our microscopic studies show that the AFQ order can influence the magnetic correlations by inducing AFM order with the same symmetry along certain magnetic field directions. Here we consider the interplay of the AFQ order and the induced symmetry-compatible AFM order via a Ginzburg-Landau theory. We show that if the induced AFM moments are allowed by symmetry, they are immediately ordered at T_Q , and the induced AFM order enhances the AFQ order by increasing T_Q with increasing magnetic field.

For simplicity, we assume that only one component of the quadrupolar moments is ordered. The ordered quadrupole and its symmetry-compatible dipolar moments are denoted as $\tau_{a(f)}$, $\sigma_{a(f)}$, and $\eta_{a(f)}$. For instance, along the magnetic field direction $\theta = \phi = 0$, the ordered moments are, respectively, O_2^0 and J^z , which correspond to τ^z , σ^z , and η^z . (In the following discussion we will only focus on the interplay of quadrupolar and dipolar moments though σ^z and η^z also include an octupolar component with the same symmetry as the dipolar component.) We then expand the Ginzburg-Landau free energy up to the fourth order of the pseudospin operators

$$\begin{aligned}
\mathcal{F} = \mathcal{F}_0 &+ \frac{1}{2} \sum_{\alpha=\tau,\sigma,\eta} [(T - T_0^\alpha)(\phi_a^\alpha)^2 + (T + T_0^\alpha)(\phi_f^\alpha)^2] + r(\tau_f\sigma_f\eta_f + \tau_f\sigma_a\eta_a + \tau_a\sigma_f\eta_a + \tau_a\sigma_a\eta_f) \\
&- H_z \sum_{c=f,a} \tau_c \left(\frac{4}{7} \sigma_c + \eta_c \right) - H_z (\sigma_f + \frac{4}{7} \eta_f) - (\delta H_\tau \tau_a + \delta H_\sigma \sigma_a + \delta H_\eta \eta_a) \\
&+ \sum_{\phi=\tau,\sigma,\eta} \frac{u_\alpha}{4} (\phi_a^\alpha)^4 + \dots
\end{aligned} \tag{3}$$

Here we have introduced staggered fields δH 's coupled to τ_a , σ_a , and η_a . For simplicity, in the free energy we neglect some quartic terms which may be allowed by symmetry, such

as $\sigma_a^2 \tau_a^2$. Including these terms will not change the results qualitatively. T_0^τ is the ordering temperature for τ_a at zero magnetic field. T_0^σ and T_0^η are ordering temperatures for magnetic dipolar moments in the absence of AFQ ordering. Here we consider the situation $T_0^{\sigma(\eta)} \leq T_0^\tau$, which is the case for $\text{Ce}_3\text{Pd}_{20}\text{Si}_6$. u_τ , u_σ , and u_η are positive coupling strengths. Note that the first term in the second line in equation (3) couples the quadrupolar moments not only to dipolar moments, but also to the magnetic field.

We obtain a set of coupled non-linear equations for $\tau_{a(f)}$, $\sigma_{a(f)}$, and $\eta_{a(f)}$ by minimizing \mathcal{F} with respect to these parameters. Solving these equations in the paramagnetic phase we have, to the leading order in H_z

$$\sigma_f \approx \frac{H_z}{T + T_0^\sigma}, \quad \eta_f \approx \frac{4H_z}{7(T + T_0^\eta)}, \quad \text{and} \quad \tau_f \approx \frac{4H_z^2(2T + T_0^\sigma + T_0^\eta - r)}{7(T + T_0^\tau)(T + T_0^\sigma)(T + T_0^\eta)}. \quad (4)$$

Now we investigate the paramagnetic to AFQ transition at a fixed H_z . Linearizing the equations for τ_a , σ_a , and η_a (by dropping the terms including u), we find that τ_a , σ_a , and η_a become nonzero only when

$$\det \begin{vmatrix} T - T_0^\tau & r\eta_f - \frac{4}{7}H_z & r\sigma_f - H_z \\ r\eta_f - \frac{4}{7}H_z & T - T_0^\sigma & r\tau_f \\ r\sigma_f - H_z & r\tau_f & T - T_0^\eta \end{vmatrix} = 0. \quad (5)$$

This determines a single temperature T_Q , at which the paramagnetic to AFQ transition takes place in the presence of magnetic field. Solving equation (5) after inserting in it equation (4), we obtain $T_Q \approx T_0^\tau + \frac{\sqrt{65}}{14}H_z$ for $T_0^\tau = T_0^\sigma = T_0^\eta$, and $T_Q \approx T_0^\tau + \frac{65}{49}H_z^2(T_0^\tau + T_0 - r)^2 / [(T_0^\tau - T_0)(T_0^\tau + T_0)^2]$ for $T_0^\tau > T_0$, where $T_0 = T_0^\sigma = T_0^\eta$. Hence we see that T_Q always increases with increasing H_z as long as $T_0^\tau \geq T_0^{\sigma(\eta)}$.

This unconventional field dependence of T_Q is due to the coupling between the quadrupolar and dipolar moments, which appears as the off-diagonal terms in equation (5). The increase of T_Q with magnetic field is consistent with the experimental phase diagram of $\text{Ce}_3\text{Pd}_{20}\text{Si}_6$. It is also compatible with the microscopically-calculated phase diagram presented in Fig.S5. It is especially instructive to note that, in Fig.S5a, T_Q increases significantly only in the O_2^0 phase, in which the AFM moment J^z is induced. By contrast, T_Q is almost unchanged in the O_{xy} phase where no magnetic moment can be induced. Note that though there is no induced dipolar moment in the O_{xy} phase along the $[0, 0, 1]$ direction, the T_{xyz} -type antiferro-octupolar moment can be induced, which gives rise to the weak field dependence of T_Q in this phase.

Equation (5) also implies that the magnetic dipolar moments immediately become ordered at T_Q , at which they are induced by the AFQ order. This conclusion survives fluctuation effects induced by the quartic couplings. The latter will renormalize the diagonal and off-diagonal terms in the matrix appearing in equation (5), which will give rise to a renormalized T_Q .

Effect of couplings to conduction electrons

The consistency between our symmetry-based analysis and microscopic calculations implies that the conclusions from the latter will survive any generalization of the model that does not change its symmetry. One important generalization of equation (2) is that the pseudospins will be Kondo-coupled to the conduction electrons. Separately, the Γ_7 doublets of the Ce ions at the $4a$ site will also be Kondo-coupled to the conduction electrons. Through the conduction electrons, the two sets of the Ce $4f$ electrons will be coupled to each other in the dipolar channel. These interactions will generate a Kondo screened ground state in the absence of a competition by RKKY interactions. The latter comprise interactions within the $4a$ and $8c$ sites, respectively, which are responsible for the AFQ and AFM orders, as well as those between $4a$ and $8c$ sites, which couple the AFM orders of the two components. The competition between the RKKY and Kondo couplings gives rise to the Kondo destruction.

References

1. Paschen, S. *et al.* Quantum critical behaviour in $\text{Ce}_3\text{Pd}_{20}\text{Si}_6$? *J. Magn. Magn. Mater.* **316**, 90–92 (2007).
2. Strydom, A. M., Pikul, A., Steglich, F. & Paschen, S. Possible field-induced quantum criticality in $\text{Ce}_3\text{Pd}_{20}\text{Si}_6$. *J. Phys.: Conf. Series* **51**, 239–242 (2006).
3. Fert, A. & Levy, P. M. Theory of the Hall effect in heavy-fermion compounds. *Phys. Rev. B* **36**, 1907–1916 (1987).
4. Paschen, S. *et al.* Hall-effect evolution across a heavy-fermion quantum critical point. *Nature* **432**, 881–885 (2004).
5. Friedemann, S. *et al.* Fermi-surface collapse and dynamical scaling near a quantum-critical point. *PNAS* **107**, 14547–14551 (2010).
6. Deen, P. P. *et al.* Quantum fluctuations and the magnetic ground state of $\text{Ce}_3\text{Pd}_{20}\text{Si}_6$. *Phys. Rev. B* **81**, 064427 (2010).
7. Goto, T. *et al.* Quadrupole ordering in clathrate compound $\text{Ce}_3\text{Pd}_{20}\text{Si}_6$. *J. Phys. Soc. Jpn.* **78**, 024716 (2009).
8. Shiina, R., Shiba, H. & Thalmeier, P., Magnetic-field effects on quadrupolar ordering in a Γ_8 -quartet system CeB_6 . *J. Phys. Soc. Jpn.* **66**, 1741-1755 (1997).
9. Ohkawa, F. J. Ordered states in periodic Anderson Hamiltonian with orbital degeneracy and with large Coulomb correlation. *J. Phys. Soc. Jpn.* **52**, 3897-3906 (1983).
10. Ohkawa, F. J. Orbital antiferromagnetism in CeB_6 . *J. Phys. Soc. Jpn.* **54**, 3909-3914 (1985).
11. Goto, T. *et al.* Ferroquadrupole ordering of the ternary intermetallic compound $\text{Ce}_3\text{Pd}_{20}\text{Ge}_6$. *Physica B* **312-313**, 492-494 (2002).
12. Nemoto, Y. *et al.*, Ferroquadrupole ordering and Γ_5 rattling motion in the clathrate compound $\text{Ce}_3\text{Pd}_{20}\text{Ge}_6$. *Phys. Rev. B* **68**, 184109 (2003).

FIG. S1: Non-Fermi liquid behaviour of $\text{Ce}_3\text{Pd}_{20}\text{Si}_6$. **a** Difference of electrical resistivity $\rho(T)$ and its residual resistivity ρ_0 vs temperature, at different magnetic fields. **b** Electronic specific heat coefficient $\Delta C/T$ vs temperature on a semi-logarithmic scale for a field of 1 T (main panel) and for several fields (inset). Both the linear T dependencies in $\rho(T)$ and the $-\ln T$ dependencies in $\Delta C/T$ are indicated by dashed lines.

FIG. S2: Fitting procedure for magnetoresistivity isotherms. Field dependence at 300 mK of the longitudinal resistivity ρ_1 , corrected for the background contribution $\rho_{1,\text{back}}$, with the sum of the two crossover functions given in the figure. The crossover positions B_N and B^* are indicated.

FIG. S3: Characteristics of the crossover at the Néel transition. Temperature dependence of the step height ΔA_N in **a** and of the crossover width w_N in **b**, determined from fits to the longitudinal and transverse resistivity ρ_1 and ρ_t , both corrected for the background contribution, and to the Hall resistivity ρ_H . The star refers to Hall resistivity data corrected for the anomalous Hall effect.

FIG. S4: Analysis of the anomalous contribution to the Hall resistivity. Measured Hall resistivity ρ_H (symbols) and fits to the data (lines through the data points), as well as the normal contribution ρ_H^0 estimated from magnetization and resistivity data as discussed in the text, vs ratio of magnetic field and crossover field B/B^* .

FIG. S5: Finite-temperature mean-field phase diagram. The parameter set is given in the text. The external magnetic field is along the directions $\theta = \phi = 0$ in **a** and $\theta = \phi = \pi/4$ in **b**. The black solid curve (T_Q) shows a continuous phase transition between the paramagnetic and the AFQ ordered phase. In **a** the blue dash dotted lines represent first-order transitions inside the AFQ phase, while in **b** the blue dash-dotted line indicates a crossover. The shaded areas refer to the magnetically ordered regimes.

TABLE I: Pseudospin representation of multipolar moments, adapted from ref.⁸. \mathbf{J} , O , and \mathbf{T} correspond to dipolar, quadrupolar, and octupolar operators, respectively. Also listed are the corresponding irreducible representations of the O_h point group.

pseudospin operator	$(\boldsymbol{\tau}, \boldsymbol{\sigma})$ representation	multipolar moment symmetry	
$\boldsymbol{\tau}'$	(τ^z, τ^x)	$\frac{1}{8}(O_2^0, O_2^2)$	Γ_3^+
$\boldsymbol{\mu}$	$2(\tau^y\sigma^x, \tau^y\sigma^y, \tau^y\sigma^z)$	$\frac{1}{2}(O_{yz}, O_{xz}, O_{xy})$	Γ_5^+
$\boldsymbol{\sigma}$	$2(\sigma^x, \sigma^y, \sigma^z)$	$\frac{7}{15}\mathbf{J} - \frac{2}{45}\mathbf{T}^\alpha$	Γ_4^-
$\boldsymbol{\eta}$	$(-\tau^z\sigma^x + \sqrt{3}\tau^x\sigma^x, -\tau^z\sigma^y - \sqrt{3}\tau^x\sigma^y, 2\tau^z\sigma^z)$	$-\frac{1}{15}\mathbf{J} + \frac{7}{90}\mathbf{T}^\alpha$	Γ_4^-
$\boldsymbol{\zeta}$	$(-\sqrt{3}\tau^z\sigma^x - \tau^x\sigma^x, \sqrt{3}\tau^z\sigma^y - \tau^x\sigma^y, 2\tau^x\sigma^z)$	$\frac{\sqrt{5}}{30}\mathbf{T}^\beta$	Γ_5^-
$\boldsymbol{\xi}$	τ^y	$\frac{\sqrt{5}}{45}T_{xyz}$	Γ_2^-

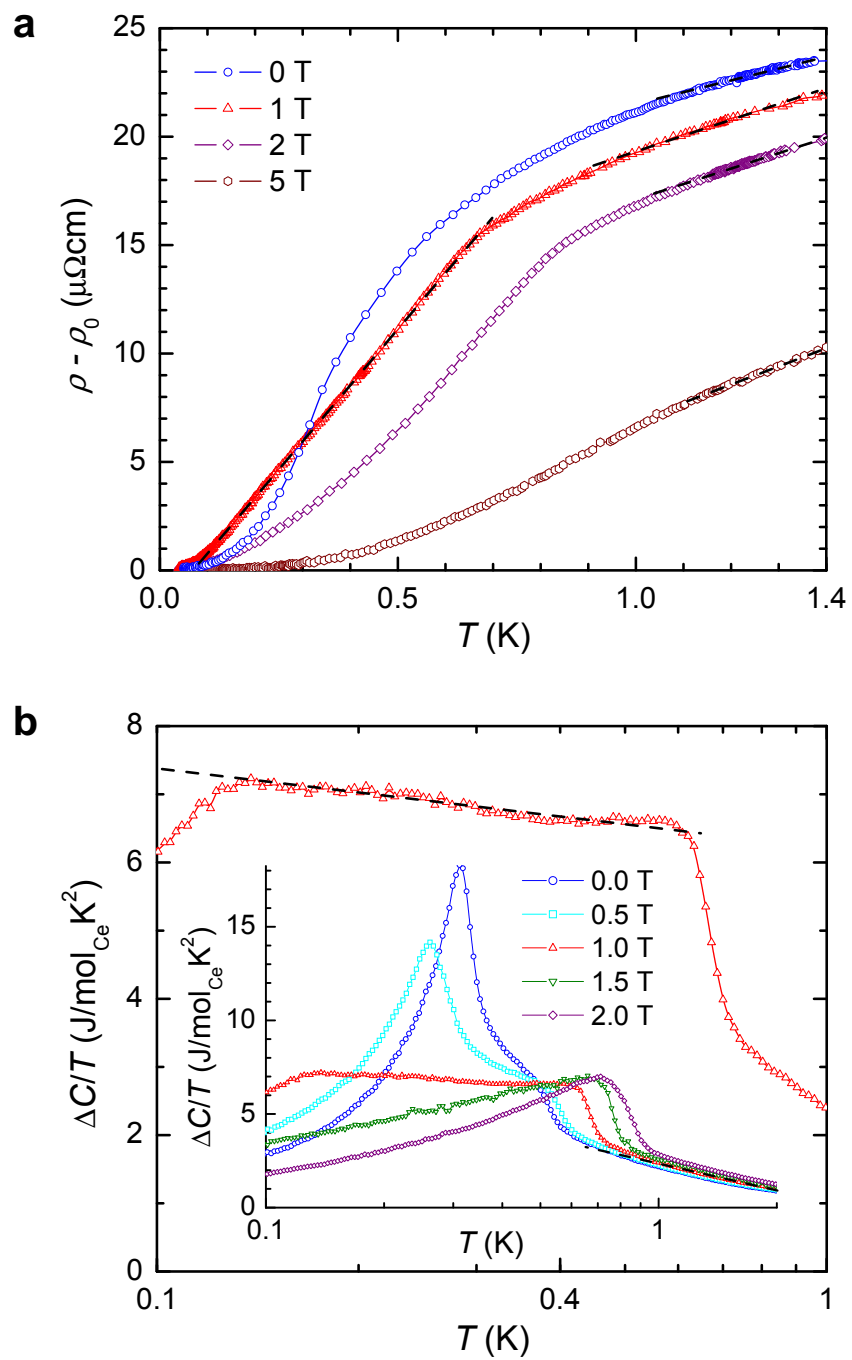


Figure S1, Supplementary Information

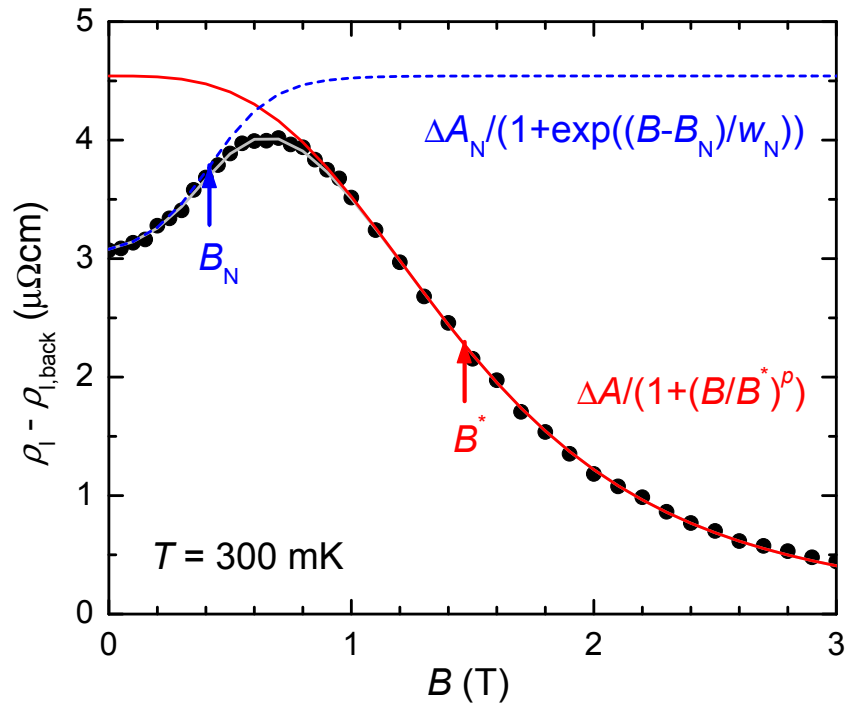


Figure S2, Supplementary Information

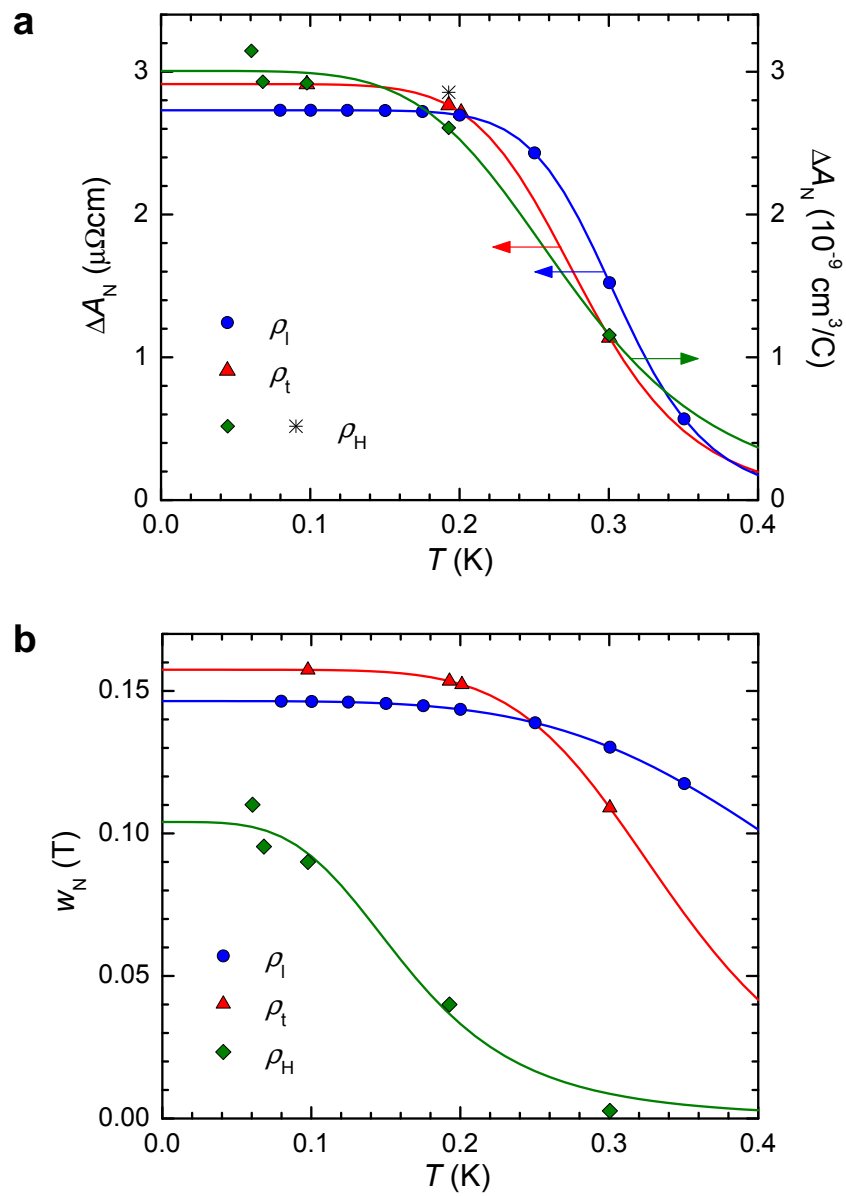


Figure S3, Supplementary Information

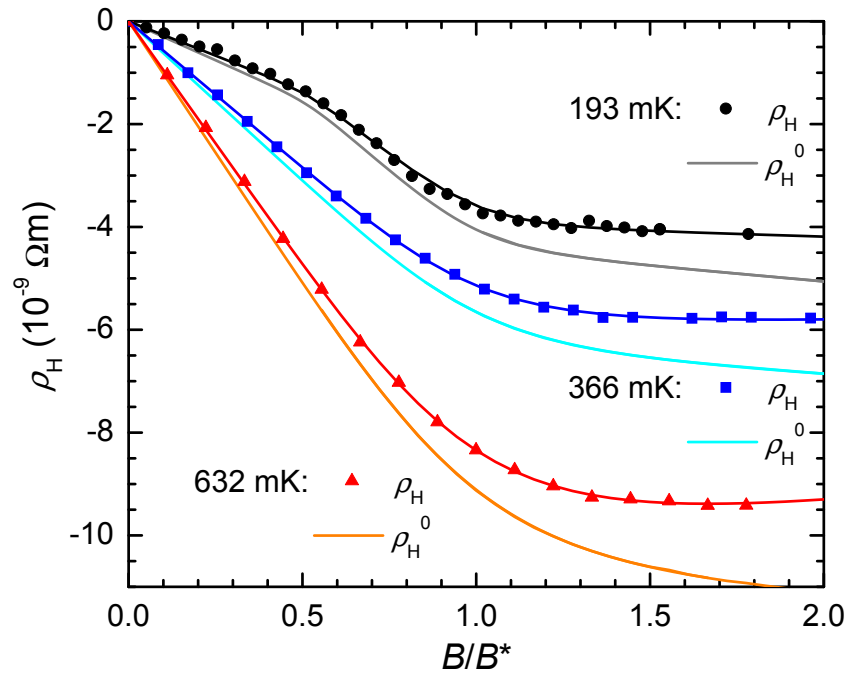


Figure S4, Supplementary Information

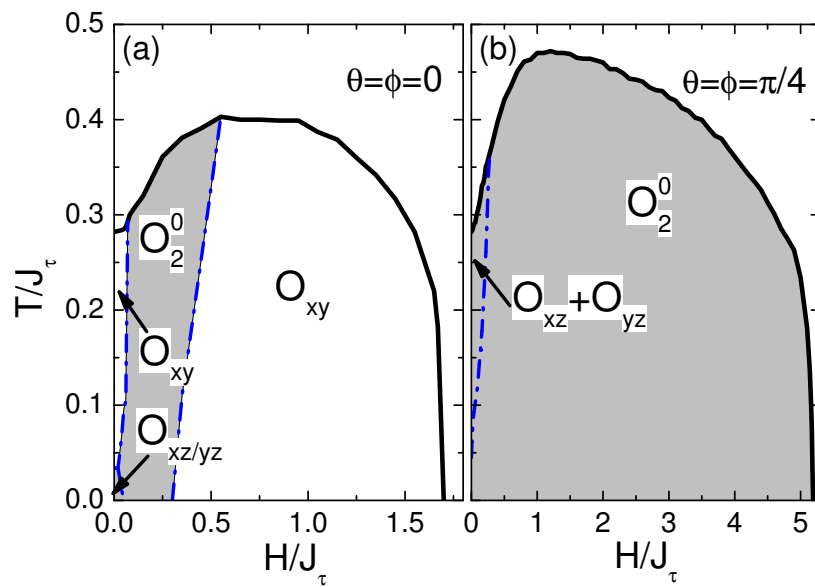


Figure S5, Supplementary Information